Gain competition in dual wavelength quantum cascade lasers

Markus Geiser,[1, 4] Christian Pflügl,[1,*] Alexey Belyanin,[2] Qi Jie Wang,[1] Nanfang Yu,[1] Tadanaka Edamura,[3] Masamichi Yamanishi,[3] Hirofumi Kan,[3] Milan Fischer,[4] Andreas Wittmann,[4] Jérôme Faist,[4] and Federico Capasso[1,5]

[1]*School of Engineering and Applied Sciences, Harvard University, 9 Oxford Street, Cambridge, Massachusetts 02138, USA*
[2]*Department of Physics, Texas A&M University, College Station, Texas 77843, USA*
[3]*Central Research Laboratories, Hamamatsu Photonics K.K., Hirakuchi 5000, Hamakita-ku, Hamamatsu 434-8601, Japan*
[4] *Institute of Quantum Electronics, ETH Zürich, CH-8093 Zürich, Switzerland*
[5]*capasso@seas.harvard.edu*
*pflugl@seas.harvard.edu

Abstract: We investigated dual wavelength mid-infrared quantum cascade lasers based on heterogeneous cascades. We found that due to gain competition laser action tends to start in higher order lateral modes. The mid-infrared mode with the lower threshold current reduces population inversion for the second laser with the higher threshold current due to stimulated emission. We developed a rate equation model to quantitatively describe mode interactions due to mutual gain depletion.

©2010 Optical Society of America

OCIS codes: (140.3070) Infrared and far-infrared lasers; (140.5965) Semiconductor lasers; (230.5590) Quantum well devices.

References and links

1. J. Faist, F. Capasso, D. L. Sivco, C. Sirtori, A. L. Hutchinson, and A. Y. Cho, "Quantum cascade laser," Science **264**(5158), 553–556 (1994).
2. S. Y. Zhang, D. G. Revin, J. W. Cockburn, K. Kennedy, A. B. Krysa, and M. Hopkinson, "λ–3.1μm room temperature InGaAs/AlAsSb/InP quantum cascade lasers," Appl. Phys. Lett. **94**(3), 031106 (2009).
3. M. Rochat, D. Hofstetter, M. Beck, and J. Faist, "Long-wavelength (λ~16 μm), room-temperature, single-frequency quantum-cascade lasers based on a bound-to-continuum transition," Appl. Phys. Lett. **79**(26), 4271 (2001).
4. A. Lyakh, C. Pflügl, L. Diehl, Q. J. Wang, F. Capasso, X. J. Wang, J. Y. Fan, T. Tanbun-Ek, R. Maulini, A. Tsekoun, R. Go, C. Kumar N. Patel, "1.6 W high wall plug efficiency, continuous-wave room temperature quantum cascade laser emitting at 4.6 µm," Appl. Phys. Lett. **92**, 111110 (2008).
5. A. Lyakh, R. Maulini, A. Tsekoun, R. Go, C. Pflügl, L. Diehl, Q. J. Wang, F. Capasso, and C. K. N. Patel, "3 Watt continuous-wave room temperature single-facet emission from quantum cascade lasers based on non-resonant extraction design approach," Appl. Phys. Lett. **95**(14), 141113 (2009).
6. R. Maulini, A. Lyakh, A. Tsekoun, R. Go, C. Pflügl, L. Diehl, F. Capasso, and C. K. N. Patel, "High power thermoelectrically-cooled and uncooled quantum cascade lasers with optimized reflectivity facet coatings," Appl. Phys. Lett. **95**(15), 151112 (2009).
7. Y. Bai, S. Slivken, S. R. Darvish, and M. Razeghi, "Room temperature continuous wave operation of quantum cascade lasers with 12.5% wall plug efficiency," Appl. Phys. Lett. **93**(2), 021103 (2008).
8. C. Gmachl, D. L. Sivco, J. N. Baillargeon, A. L. Hutchinson, F. Capasso, and A. Y. Cho, "Quantum cascade lasers with a heterogeneous cascade: two-wavelength operation," Appl. Phys. Lett. **79**(5), 572 (2001).
9. R. Maulini, A. Mohan, M. Giovannini, J. Faist, and E. Gini, "External cavity quantum-cascade laser tunable from 8.2 to 10.4 µm using a gain element with a heterogeneous cascade," Appl. Phys. Lett. **88**(20), 201113 (2006).
10. A. Hugi, R. Terazzi, Y. Bonetti, A. Wittmann, M. Fischer, M. Beck, J. Faist, and E. Gini, "External cavity quantum cascade laser tunable from 7.6 to 11.4 µm," Appl. Phys. Lett. **95**(6), 061103 (2009).
11. E. Rosencher, A. Fiore, B. Vinter, V. Berger, Ph. Bois, and J. Nagle, "Quantum engineering of optical nonlinearities," Science **271**(5246), 168–173 (1996).
12. C. Sirtori, F. Capasso, J. Faist, L. N. Pfeiffer, and K. W. West, "Far-infrared generation by doubly resonant difference frequency mixing in a coupled quantum well two-dimensional electron gas system," Appl. Phys. Lett. **65**(4), 445 (1994).
13. N. Owschimikow, C. Gmachl, A. Belyanin, V. Kocharovsky, D. L. Sivco, R. Colombelli, F. Capasso, and A. Y. Cho, "Resonant second-order nonlinear optical processes in quantum cascade lasers," Phys. Rev. Lett. **90**(4), 043902 (2003).

14. M. Austerer, C. Pflügl, S. Golka, W. Schrenk, A. M. Andrews, T. Roch, and G. Strasser, "Coherent 5.35 µm surface emission from a GaAs-based distributed feedback quantum-cascade laser," Appl. Phys. Lett. **88**(12), 121104 (2006).
15. M. A. Belkin, F. Capasso, A. Belyanin, D. L. Sivco, A. Y. Cho, D. C. Oakley, C. J. Vineis, and G. W. Turner, "Terahertz quantum-cascade-laser source based on intracavity difference-frequency generation," Nat. Photonics **1**(5), 288–292 (2007).
16. M. A. Belkin, F. Capasso, F. Xie, A. Belyanin, M. Fischer, A. Wittmann, and J. Faist, "Room temperature terahertz quantum cascade laser source based on intracavity difference-frequency generation," Appl. Phys. Lett. **92**(20), 201101 (2008).
17. C. Pflügl, M. A. Belkin, Q. J. Wang, M. Geiser, A. Belyanin, M. Fischer, A. Wittmann, J. Faist, and F. Capasso, "Surface-emitting terahertz quantum cascade laser source based on intracavity difference-frequency generation," Appl. Phys. Lett. **93**(16), 161110 (2008).
18. J. Faist, D. Hofstetter, M. Beck, T. Aellen, M. Rochat, and S. Blaser, "Bound-to-continuum and two-phonon resonance quantum-cascade lasers for high duty cycle, high-temperature operation," IEEE J. Quantum Electron. **38**(6), 533–546 (2002).
19. A. Belyanin, M. Troccoli, and F. Capasso, "Raman Injection and Inversionless Intersubband Lasers" in *Intersubband Transitions in Quantum Structures*, R. Paiella (McGraw-Hill Companies, 2006), chapter 6.3.5.

1. Introduction

Quantum cascade lasers [1] (QCLs) are semiconductor lasers based on intersubband transitions between electronic states in coupled quantum wells (QWs). The transition wavelength is a function of the QW and barrier widths in the active region and can be designed over a broad spectral range for a given material. Mid-infrared (mid-IR) QCLs working at room temperature (RT) have been demonstrated in the spectral range from about 3µm [2] to 15µm [3] and Watt-level output power in continuous wave operation was reported [4–7]. A unique feature of these devices is the cascading scheme, in which electrons traverse a stack of many, typically 30-50 active regions. Due to the flexibility in design, QCLs featuring heterogeneous cascades can be realized, which lase in several wavelength bands simultaneously [8]. Heterogeneous active regions are also employed in broadband tunable lasers for spectroscopic applications [9,10]. Besides the advantage of delivering multiple wavelengths simultaneously, these devices are also very interesting for nonlinear light generation in QCLs. Giant nonlinearities in semiconductor QW structures have been predicted [11] and experimentally demonstrated [12]. Integration of coupled QWs with a large nonlinear susceptibility in the active region of QCLs has led to the demonstration of intracavity second harmonic [13,14] and sum-frequency generation [13] in QCLs. Recently, difference frequency generation (DFG) has been demonstrated in dual wavelength mid-IR QCLs [15,16]. Two mid-IR pump beams sharing the same waveguide generate their difference-frequency in the THz regime by means of intersubband nonlinearities integrated in the active regions of these devices. For efficient DFG a large overlap of the two pump beams is desired, as DFG power is proportional to the product of their intensities. In recent work, we found that the two pump lasers tend to operate in different lateral modes, leading to reduced efficiency in nonlinear light generation [17]. In this paper we study in detail the multimode behavior of dual wavelength QCLs and describe the experimental effects by a rate equation model which includes the interaction of the two lasers.

2. Active region and waveguide design

We investigated two slightly different dual wavelength mid-IR QCL designs. The active region of the first structure (S1) consists of two stacks of stages with their band structures shown in Fig. 1. The first stack is based on a double phonon resonance (DPR) design [18] lasing at about 10.5µm (Fig. 1(a), main laser transition: green-red) and the second stack features a bound-to-continuum (BTC) design [18] lasing at about 8.9µm (Fig. 1(b), main laser transition: green-blue). As described in detail in [16], the BTC design also includes a large nonlinear susceptibility $\chi^{(2)}$ for efficient generation of the difference-frequency of the two mid-IR lasers. To obtain a large value for $\chi^{(2)}$, the lasing transition of the DPR laser is close to resonance (difference is ~5 meV) with the transition $4 \rightarrow 3$ (see Fig. 1 (b) and (d) transition green-red) in the BTC design.

Figure 1(c) shows a schematic of the waveguide. 30 stages of each active region including thin low-doped InGaAs layers surrounding the active regions were grown on a low doped ($\sim1*10^{17}$cm^{-3}) InP wafer consecutively, followed by a 3.5µm thick cladding layer ($\sim5*10^{16}$cm^{-3}) and a 200nm thick highly doped plasmon layer ($\sim5*10^{18}$cm^{-3}). This dielectric waveguide confines both mid-IR modes in the vertical direction [16].

A second structure (S2) was grown with the same waveguide and a very similar active region design. The only difference was that the layers in the active region were about 10% thicker than the ones in the original wafer and the active region doping was lower. This led to a different performance as discussed in detail in section 4.
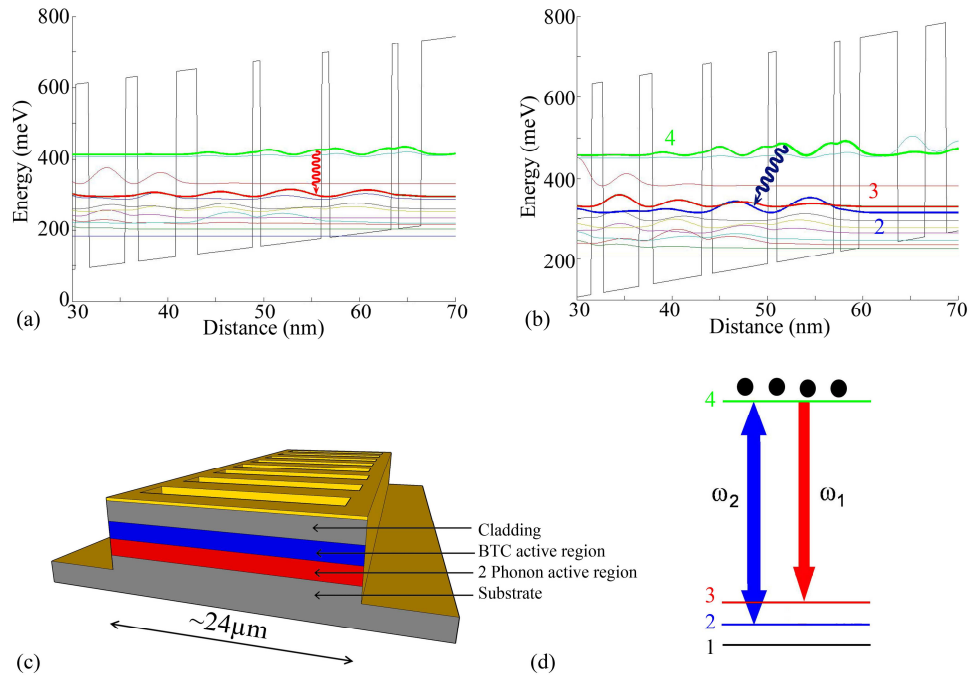

Fig. 1. Band diagram for (a) the double phonon resonance and (b) the bound to continuum active region of structure S1 calculated for an applied field of 34KV/cm and 41kV/cm, respectively which are the injection resonance conditions for each active region. The lasing transitions ((a) green-red, (b) green-blue) are shown with wavy arrows. The layer sequence in nm, starting from the injection barrier, for the BTC structure is <u>4.0</u>/ 2.4/ <u>0.7</u>/ 6.5/ <u>0.8</u>/ 6.4/ <u>0.8</u>/ 5.8/ <u>2.2</u>/ 4.0/ <u>1.3</u>/ 3.8/ <u>1.4</u>/ 3.7/ <u>1.5</u>/ 3.6/ <u>1.9</u>/3.6 / <u>2.5</u>/ 3.6/ <u>2.5</u>/ 3.5. The layer sequence for one period of a DPR section is <u>4.0</u>/2.0/ <u>0.7</u>/ 6.0/ <u>0.9</u>/ 5.9/ <u>1.0</u>/ 5.2/ <u>1.4</u>/ 3.8/ <u>1.2</u>/ 3.2/ <u>1.2</u>/ 3.2/ <u>1.6</u>/ 3.1/ <u>1.9</u>/ 3.1/<u>2.2</u>/ 3.0/ <u>2.2</u>/ 2.9. The barriers are underlined. (c) Cross sectional view of the ridge showing schematically the waveguide design. (d) Schematic energy diagram of the BTC active region with states 4, 3, and 2. State 1 is the injector ground state. States 4, 3 and 2 are marked in bold green, red and blue in (b), respectively. Radiation ω_1 (green to red) comes from the DPR laser (Fig. 1a).

3. Device processing and measurement techniques

The devices were processed into ridge waveguide lasers. The processing started with reactive ion etching of 20-28µm wide ridges. We also processed narrower devices (12-18µm) which were wet etched. A 300nm thick Silicon Nitride insulation layer was deposited and opened on top of the ridge. After that, extended Ti/Au contacts were evaporated. The wafers were thinned to approximately 250µm and cleaved into laser bars, which were Indium mounted on Copper heat sinks and wire bonded. Some of the devices had a second-order grating for THz surface emission etched into the top of the ridges since they were used for the work discussed in [17], which also includes a detailed description of their fabrication. This grating is designed

to couple efficiently to the generated THz radiation and is expected to have only little influence on the mid-IR modes. For electroluminescence measurements, circular mesa structures were processed with wet etched sidewalls to eliminate cavity feedback.

For the laser measurements, our devices were operated in pulsed mode with 60ns pulses at a 20kHz repetition rate. The lasers were mounted in Nitrogen flow cryostats. Mid-IR spectra were taken with a Fourier transform IR spectrometer (FTIR). 1D far fields were collected with a Mercury-Cadmium-Telluride (MCT) detector, which is mounted on a motorized rotation stage and rotated around the sample. 2D far fields are composed of multiple 1D far fields. A 9.5µm short pass filter was placed in front of the detector to measure the far field of the short wavelength pump beam separately. The far field of the long wavelength pump beam was obtained by subtracting the short wavelength far field from the far field measured without filter.

Electroluminescence (EL) data was collected with a liquid Nitrogen cooled MCT detector, using lock-in technique and a FTIR spectrometer operated in step scan mode.

4. Device performance and far field behavior

The devices fabricated from the first wafer S1, showed lasing at two wavelengths up to RT. We observed sets of longitudinal modes around 10.5µm and 8.9µm corresponding to the peaks of the gain spectrum of the DPR and BTC active regions, respectively. In the following, we refer to the set of modes lasing at ~10.5µm and to the set of modes lasing at ~8.9µm as the DPR laser and the BTC laser, respectively since the main contribution to lasing at these wavelengths is made by the respective active regions. The DPR laser has a lower threshold current density than the BTC laser and typically also a significantly larger slope efficiency. A typical set of data – mid-IR spectra, light vs. current and voltage vs. current characteristics of a 28µm wide and 1.5mm long device are shown in Fig. 2. EL measurements show comparable peak intensities for both wavelengths (see Fig. 3) over a large range of applied voltages, which indicates that the significant difference in performance of the two lasers cannot be explained by large differences in gain for the two lasers.
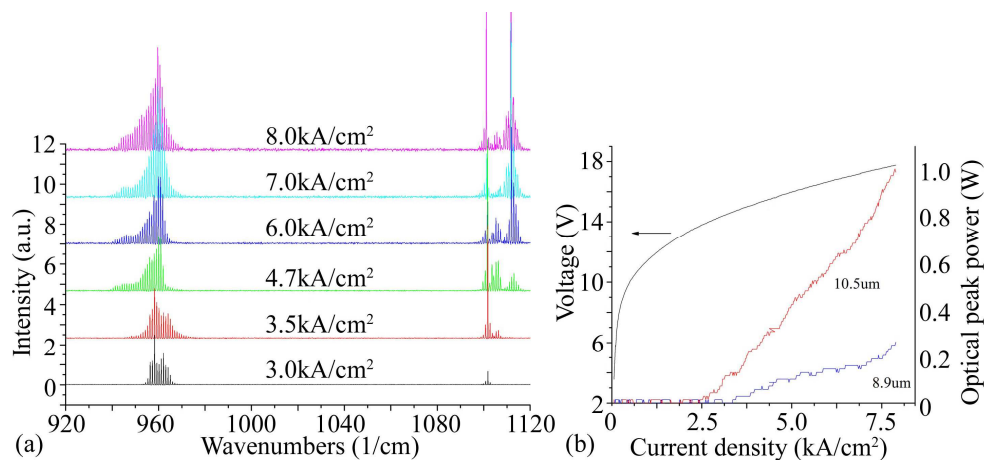

Fig. 2. IR-characterization of a typical device of structure S1, taken at a temperature of 150K. (a) shows the spectra at different current densities. The spectra are shifted vertically for clarity. Light output vs. current density and voltage vs. current density characteristics of the same device can be seen in (b).
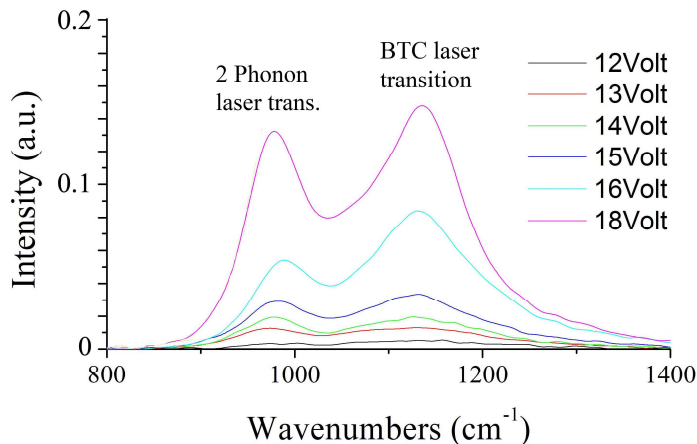
Fig. 3. EL spectra of structure S1 at different voltages, taken from mesa structures at 78K. The two laser transitions of the two different active regions can be distinguished.

We measured the far field profile of several devices at different temperatures. Figure 4 shows a 2D far field of the mid-IR emission. All of the lasers with a ridge width equal to or larger than 20µm showed lasing in TM_{00} mode for the DPR laser and higher order lateral mode operation (typically TM_{02} or TM_{03}) for the BTC laser, except for one device, which showed TM_{00} operation for both wavelengths. Only for very narrow devices (~12µm wide), both pump beams lased consistently in TM_{00}. Observed differences in performance (e. g. appearance of different higher order modes) between nominally identical devices can be explained by losses due to sidewall roughness scattering which can vary from device to device. In narrower ridges, where only TM00 modes are present, higher order modes overlap significantly with the lossy SiN insulation layer at the sidewall of the ridges, which suppresses the appearance of these modes.
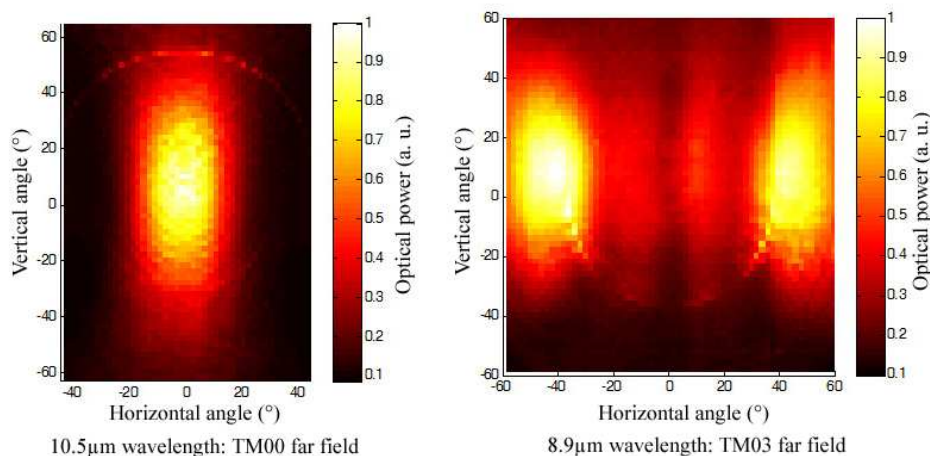

10.5µm wavelength: TM00 far field

8.9µm wavelength: TM03 far field

Fig. 4. 2D far field profile for a typical device from wafer S1 with the DPR laser operating in TM_{00} and the BTC laser in TM_{03}, taken at a temperature of 78K.

The devices fabricated from the second wafer (S2) showed a slightly different behavior. These devices emitted around 10.2µm (DPR laser) and 8.8µm (BTC laser). The threshold current density for the DPR laser was lower at low temperatures, but the difference between the thresholds of the two lasers was smaller than in the devices processed from the first wafer.

Experimental data shows, that threshold current densities rise slightly slower with temperature for the BTC laser than for the DPR laser. This leads to threshold inversion in a particular 24µm wide sample at approx. *120K*, resulting in the BTC laser having a lower J_{th} above this temperature.

Below 120K the far field characteristics of this device are similar to the farfield characteristics of devices from wafer S1: the device operates in TM_{00} mode for the DPR laser and TM_{02} for the BTC laser (see Fig. 5a). Above 120K, however, when the BTC laser has a lower threshold current density than the DPR laser, both lasers operate in TM_{00} mode (Fig. 5b).
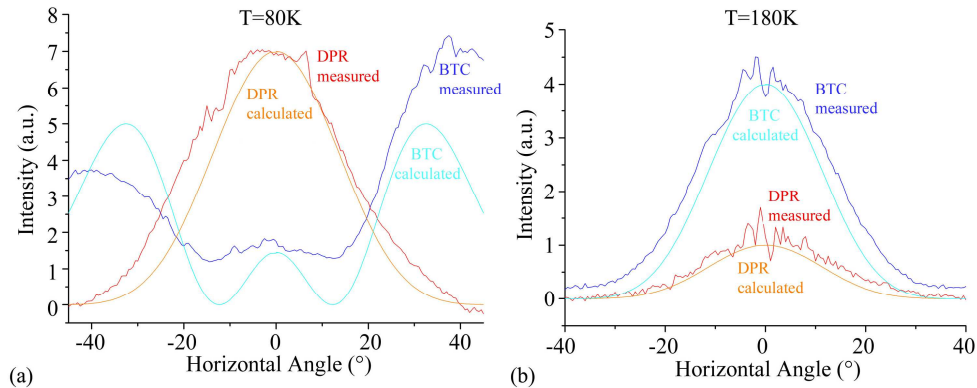

Fig. 5. Far field profile for a device of structure S2, taken at (a) 80K and (b) 180K. While the 10.2µm DPR laser operates at both temperatures in the TM_{00} mode, the 8.8µm BTC laser changes from TM_{02} to TM_{00} with increasing temperature. The asymmetry of the *BTC* mode in (a) is attributed to a not perfectly horizontally mounted sample.

This result indicates that the high intracavity photon density around 10.5µm influences the performance and the properties of the BTC active region. If the threshold current for the DPR laser is lower than the one of the BTC laser, the high intracavity intensity at around 10.5µm leads to the reduction of the electron population in the upper laser state of the BTC active region due to stimulated emission, because this design has transitions that are close to resonance with the DPR laser mode. This reduces population inversion in the BTC stack and degrades the performance of the 8.9µm pump beam, while the BTC active region contributes to lasing around 10.5µm. This effect depends on the intracavity photon density and is therefore strongest in the center of the ridge device, where the 10.5µm TM_{00} mode has its intensity maximum. This leads to a stronger reduction of the gain in the center of the ridge compared to the edges of the ridge, favoring lasing in higher order modes of the BTC laser.

In the next section we present a rate equation model which can numerically explain this behavior.

5. Rate equation model

We use steady state rate Eqs. (1) – (4) to model the position dependent electron population of the different states in the BTC active region. The rate equations describe four energy levels shown in Fig. 1(d): an upper laser state (4), a lower laser state (2), a state almost in resonance with the 10.5µm radiation (3) and state (1), which includes the additional active region and injector states. As we are interested in the electron population of these states below threshold of the BTC laser, we neglect the effect of the radiation at 8.9µm on the electron populations and include only the stimulated transitions due to the presence of the 10.5µm DPR laser mode in the cavity. This intensity is deduced from experimental data. The rate of stimulated transitions is dependent on the 10.5µm photon density, and therefore on the position in the BTC active region. The most significant contribution to the gain reduction is caused by the transition between the upper laser state 4 and state 3. Additionally, stimulated transitions to other levels have to be included. For the present active region, the only other considerable

contribution is caused by transitions from state 4 to the lower laser level 2. The rate equations are:

$$\frac{dn_4(x,y)}{dt} = \frac{j_{inject}}{q} - \frac{n_4(x,y)}{\tau_{4nonrad.}} - \sigma_1 S(x,y)(n_4(x,y) - n_3(x,y)) - \sigma_2 S(x,y)(n_4(x,y) - n_2(x,y)) = 0, \quad (1)$$

$$\frac{dn_3(x,y)}{dt} = \frac{n_4(x,y)}{\tau_{43}} + \sigma_1 S(x,y)(n_4(x,y) - n_3(x,y)) - \frac{n_3(x,y)}{\tau_{3nonrad.}} = 0, \quad (2)$$

$$\frac{dn_2(x,y)}{dt} = \frac{n_4(x,y)}{\tau_{42}} + \frac{n_3(x,y)}{\tau_{32}} - \frac{n_2(x,y)}{\tau_{21}} + \sigma_2 S(x,y)(n_4(x,y) - n_2(x,y)) = 0, \quad (3)$$

$$\frac{dn_1(x,y)}{dt} = \frac{n_4(x,y)}{\tau_{41}} + \frac{n_3(x,y)}{\tau_{31}} + \frac{n_2(x,y)}{\tau_{21}} - \frac{j_{inject}}{q} = 0, \quad (4)$$

where j_{inject} is the injection current density, τ_{ij} are the transition lifetimes from state i to state j, $\tau_{i\ nonrad}$ is the total nonradiative lifetime of state i and n_i is the local sheet carrier density in state i. x and y describe the spatial position within the device cross-section as explained below. S(x, y) is the photon flux density with a spatial distribution which is determined by the TM_{00} mode profile of the cold cavity at 10.5µm wavelength. σ_1 and σ_2 are the cross sections for stimulated transitions from the upper state 4 to the states 3 and 2 respectively. They are defined in Eq. (5):

$$\sigma_1 = \frac{2\pi e^2 z_{43}^2}{\varepsilon_0 n\lambda L_p} \frac{2\gamma_{43}}{(E-E_{43})^2 + (2\gamma_{43})^2}, \sigma_2 = \frac{2\pi e^2 z_{42}^2}{\varepsilon_0 n\lambda L_p} \frac{2\gamma_{42}}{(E-E_{42})^2 + (2\gamma_{42})^2} \quad (5)$$

Here, e is the elementary charge, z_{ij} is the dipole matrix element for the transition i → j, n is the effective refractive index of the 10.5µm mode, λ is the vacuum wavelength, L_p is the thickness of one stage in the active region (60nm), γ_{ij} is the half width at half maximum (HWHM) of the respective transition i → j (in our model we assumed γ_{ij} = 7.5meV for the mid-IR transitions 4-3 and 4-2), E is the energy of the 10.5µm photons and E_{ij} is the energy difference between states i and j.

We calculated the following nonradiative lifetimes at RT: $\tau_{4\ nonrad}$ = *1*ps, τ_{43} = *12.5*ps, τ_{42} = *2.3*ps, τ_{41} = *2.1*ps, $\tau_{3\ nonrad.}$ = *0.13*ps, τ_{32} = *3.0*ps, τ_{31} = *0.15*ps and τ_{21} = *0.18*ps. These calculated lifetimes are based on LO-phonon scattering at an applied field of 33kV/cm (corresponds to the threshold voltage of the BTC laser). Matrix elements are: z_{43} = *1.57*nm and z_{42} = *1.80*nm. The photon flux density of the 10.5µm mode is deduced from the measured edge emission power of a typical device slightly below the threshold current density of the BTC laser.

The equations are solved for each of the 30 stages of the BTC active region (y-direction) and for 100 lateral positions across the ridge (x-direction) for each stage. This divides the BTC active region into *3000* pixels. The injection current density of 6kA/cm^2 used in the model is higher than the 10.5µm DPR laser threshold current density at RT and lower than the threshold current density for the 8.9µm BTC laser. Figure 6 shows the calculated spatially dependent population inversion in the BTC active region in the presence of the 10.5µm TM_{00} mode of intracavity power corresponding to 30mW facet emission in a 24µm wide ridge.
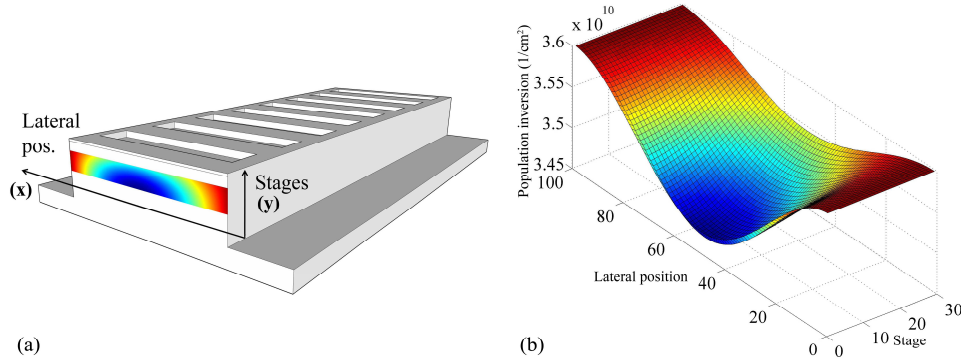
Fig. 6. Position dependent population inversion in the BTC active region. Depopulation via stimulated emission of the 10.5 μm photons is strongest in the middle of the ridge, where their density is the highest. (a) is a schematic, while (b) quantifies the effect.

The gain for the different lateral modes TM_{0a}, a = 0, 1, 2,... of the 8.9μm laser is given by the sum of the contributions of each pixel $g_{TM0a}(x,y)$, x = 1…100, y = 1…30. The gain for one pixel is shown in Eq. (6):

$$g_{TM0a}(x,y) = \frac{\omega_{8.9\mu m} e^2 z_{42}^2}{\varepsilon_0 \hbar c n \, L_p} \Gamma_{TM0a}(x,y) \times \frac{1}{2} \Re \left\{ \frac{\frac{1}{G_{42} + |\Omega(x,y)|^2 / G_{32}} \times}{\left[\frac{|\Omega(x,y)|^2 \, (n_3(x,y) - n_4(x,y))}{G_{32} G_{43}} + (n_4(x,y) - n_2(x,y)) \right]} \right\} \quad (6)$$

The gain term includes the usual intersubband gain, as well as a contribution from an Anti-Stokes Raman scattering of the 10.5μm laser mode into the 8.9μm laser mode [19]. Note that the scattering involves emission or absorption of the intersubband polariton resonant to the transition 2-3 (see Fig. 1b and 1d); it does not involve phonons. The absolute value of the Raman contribution is approximately one third of the total value of the gain but has a negative sign because population of the upper laser state 4 is higher than that of state 3. Here, $\omega_{8.9\mu m}$ is the angular frequency of the $8.9\mu m$ mode, e is the elementary charge, z_{42} is the dipole transition matrix element from 4 to 2, c is the speed of light in vacuum, n is the effective refractive index, L_p is the thickness of one stage in the active region (60nm) and $\Gamma_{TM0a}(x,y)$ is the overlap of the transversal mode TM_{0a} with the current pixel. Furthermore, Eq. (7)

$$G_{ij} = \gamma_{ij} + i \left(\Delta E_{ij} / \hbar - \omega_{ij} \right) \quad (7)$$

defines the complex detunings, with γ_{ij} being the HWHM of the transition between states i and j (7.5meV for the mid-IR transitions 4→2 and 4→3 and 0.75meV for the 3→2 transition), ΔE_{ij} is the energy difference between levels i and j. $\Omega(x,y) = e z_{34} E_{\omega 1}(x,y)/\hbar$ is the Rabi frequency, where $E_{\omega 1}(x,y)$ is the electric field in the 10.5μm laser mode.

The total modal gain for each mode is now determined by summing over all pixels. Table 1 shows the resulting gain values in cm^{-1} for different lateral modes for a 24μm wide ridge as shown in Fig. 6. The total modal gain for the 8.9μm mode was calculated in the presence and without a 10.5μm mode.

If no 10.5μm radiation is present, higher order modes have slightly higher modal gain. The small differences are due to different effective refractive indices for different modes. Higher order modes also have higher waveguide losses as they overlap more with the lossy SiN insulation layer at the sidewall of the ridges. The difference in waveguide loss for the TM_{00} and TM_{03} mode for example was calculated to be ~1.25cm^{-1} with the TM_{00} mode having lower losses. The difference in waveguide losses is larger than the difference in gain, leading to a larger net gain (modal gain minus waveguide losses) for the TM_{00} mode compared to higher order modes.

In the presence of 10.5μm radiation, however, the modal gain for the 8.9μm mode is reduced due to stimulated emission as discussed above. This reduction depends on the intracavity photon intensity of the 10.5µm TM_{00} mode and is smaller for higher order modes than for the TM_{00} mode. This effect increases the difference in modal gain for different modes. Table 1 shows that already for small photon intensities –corresponding to an output power of 30mW at 10.5µm - the difference between the TM_{00} and TM_{03} mode is about ~2cm-1. This difference overcompensates for the larger waveguide losses for the higher order mode, leading to a higher net gain for the TM_{03} mode compared to the TM_{00} mode. This is in accordance with our experimental results which show higher order mode operation for the 8.9µm mode in broad ridges (>20µm).in the presence of 10.5µm radiation.

Table 1. Modal Gain for Different Lateral Modes With and Without 10.5µm Radiation [a]

Mode	TM_{00}	TM_{01}	TM_{02}	TM_{03}
No radiation at 10.5 μm	20.04	20.08	20.25	20.49
30mW radiation at 10.5 μm	15.07	16.61	16.83	17.03

[a] Calculated gain in cm^{-1} for the different lateral modes without and with the presence of a 10.5µm mode. The simulated device is 24µm wide and 2mm long.

6. Summary and conclusions

We performed a detailed experimental study of the lateral mode behavior of dual wavelength QCLs, comprising heterogeneous active regions. Unexpected and disadvantageous appearance of higher order lateral modes was observed. To describe and understand the underlying physics we suggest a rate equation model that includes the mutual interactions of the two laser modes. Based on these assumptions about electronic population of the active region obtained by the rate equation model, the gain for different lateral modes can be calculated. In this model, the mid-IR mode with the lower lasing threshold current would reduce population inversion in the laser with the higher threshold current due to stimulated emission. This effect is more pronounced in the center of the ridge where the lower threshold mode, which typically is TM_{00}, has its intensity maximum. This leads to a stronger reduction of the gain in the center of the ridge compared to the outer parts of the ridge, favoring lasing in higher lateral modes of the second wavelength. The predictions of this model match the experimental findings. The model developed in this work can also be expanded to any type of multi-wavelength and broadband QCL based on heterogeneous cascades which are interesting for many applications such as sensing.